The Astrophysical Journal, 662:701–714, 2007 June 10
© 2007. The American Astronomical Society. All rights reserved. Printed in U.S.A.
Ⓔ

SHELL MODELS OF RMHD TURBULENCE AND THE HEATING OF SOLAR CORONAL LOOPS

E. Buchlin[1,2] and M. Velli[1,3]

Received 2006 June 24; accepted 2007 January 11

ABSTRACT

A simplified nonlinear numerical model for the development of incompressible magnetohydrodynamics in the presence of a strong magnetic field $\boldsymbol{B}_\|$ and stratification, nicknamed "Shell-Atm," is presented. In planes orthogonal to the mean field, the nonlinear incompressible dynamics is replaced by two-dimensional shell models for the complex variables u and b, allowing one to reach large Reynolds numbers while at the same time carrying out sufficiently long integrations to obtain good statistics at moderate computational cost. The shell models of different planes are coupled by Alfvén waves propagating along $\boldsymbol{B}_\|$. The model may be applied to open or closed magnetic field configurations where the axial field dominates and the plasma pressure is low; here we apply it to the specific case of a magnetic loop of the solar corona heated by means of turbulence driven by photospheric motions, and we use statistics for its analysis. The Alfvén waves interact nonlinearly and form turbulent spectra in the directions perpendicular and, through propagation, also parallel to the mean field. A heating function is obtained and shown to be intermittent; the average heating is consistent with values required for sustaining a hot corona and is proportional to the aspect ratio of the loop to the -1.5 power, and characteristic properties of heating events are distributed as power laws. Cross-correlations show a delay of dissipation compared with energy content.

Subject headings: MHD — Sun: corona — Sun: flares — turbulence

Online material: color figures

1. INTRODUCTION

Magnetohydrodynamic (MHD) turbulence in the presence of a mean magnetic field, with or without density and gravitational gradients, plays a role in many environments, ranging from stellar coronae and winds (Klein et al. 1991) to the interstellar medium (Desai et al. 1994) and accretion disks. In such regions, energy may be transferred, accumulated, and dissipated in a way that is inherently anisotropic (Shebalin et al. 1983; Oughton et al. 1994; Kinney & McWilliams 1998; Müller et al. 2003; Oughton et al. 2004).

In particular, in solar coronal physics, where one of the main problems is to understand how the corona can be sustained at more than a million kelvins, it is believed that the necessary heating could be produced at small scales generated by a nonlinear cascade along a turbulent spectrum (Heyvaerts & Priest 1992; Gómez & Ferro Fontán 1992). Furthermore, as flux tubes (e.g., in the form of coronal loops or coronal funnels) are omnipresent, the anisotropy coming from the dominant magnetic field may be a central feature of the processes governing energy dissipation, such as the nonlinear collisions of counterpropagating Alfvén wave packets. It can thus be expected that solving the coronal heating problem, that is, understanding how the temperature of the corona can be sustained, may require one to understand the details of the turbulent dynamics of MHD in these environments.

One way to study and the dynamics of such systems is to perform direct numerical simulations (DNSs). In the case of anisotropic MHD, DNSs have provided insight into subjects such as the anisotropy of the spectra (e.g., Kinney & McWilliams 1998; Oughton et al. 2004), the parametric decay of Alfvén waves (e.g., Del Zanna et al. 2001), and Alfvén wave filamentation (e.g., Passot & Sulem 2003). MHD simulations are also used to study the topology of magnetic field lines and magnetic reconnection in the corona (e.g., Aulanier et al. 2005). But the Reynolds numbers attained in all the DNSs up to now are below 10^3, while they are believed to be 10^{12}–10^{14} in the corona. DNSs are very far from being able to represent all the scales of turbulence in the corona; there is a huge gap to fill. Furthermore, as statistics are of great help in the study of turbulence, attempts have been made to statistically analyze energy dissipations produced by DNSs. Distributions of events have been, for instance, presented by Dmitruk et al. (1998) and Georgoulis et al. (1998) from two-dimensional DNSs of reduced MHD. But it is still difficult to get significant statistics from three-dimensional DNSs, and it is even more difficult when trying to go to higher Reynolds numbers, because then the grid resolution must be higher and the computations of the model are too slow. For all these reasons, there is a need for simplified numerical models of MHD that can run sufficiently fast to get statistics of turbulence at high Reynolds numbers while retaining the most relevant features of MHD turbulence.

Several approaches have been used to build such simplified numerical models of MHD. For example, the self-organized criticality (SOC) behavior of MHD systems can be modeled with cellular automata, where the interactions of individual cells translate into a global statistical behavior of the whole system, following the first models of Lu & Hamilton (1991) and Lu et al. (1993). However, the need for physical realism is not entirely addressed by the cellular automata, despite efforts to include the constraints that issue from the MHD equations (Vlahos et al. 1995; Isliker et al. 2000, 2001; Buchlin et al. 2003).

Another approach is to simplify the nonlinear interactions by reducing the number of modes that are allowed to interact nonlinearly. In the context of coronal loops, a shell-model approach has been used by Nigro et al. (2004, 2005). We have developed a similar numerical model independently, starting from the reduced MHD equations but allowing for stratification of the plasma. This

---

[1] Dipartimento di Astronomia e Scienza dello Spazio, Università di Firenze, I-50125 Florence, Italy.

[2] Space and Atmospheric Physics Group, Blackett Laboratory, Imperial College London, London SW7 2BW, UK.

[3] Jet Propulsion Laboratory, California Institute of Technology, Pasadena, CA 91109.

numerical code, nicknamed "Shell-Atm," allows one to reach (kinetic and magnetic) Reynolds numbers unachieved before. In this paper, we focus on the problem of a coronal loop where energy is forced into the system by footpoint motions, describing in detail the dynamics of the heating events, turbulence spectra, statistics, and scaling laws.

2. DESCRIPTION OF THE SHELL-ATM MODEL

We start from an approximation to incompressible MHD known as reduced MHD (RMHD; Kadomtsev & Pogutse 1974; Strauss 1976), which is valid when the plasma β-parameter (kinetic over magnetic pressure) is low, the domain has a large aspect ratio ($a = l/L \ll 1$), and the poloidal field is small compared with a strong axial external $\boldsymbol{B}_\parallel$ magnetic field ($B_\perp/B_\parallel \lesssim a$). In this approximation, the largest extension L of the domain defines the parallel direction, or z-axis, and the velocity field is only composed of fluctuations $\boldsymbol{u}_\perp$ orthogonal to the z-axis; the magnetic field can be decomposed into $\boldsymbol{B}_\parallel + \boldsymbol{B}_\perp$, where $\boldsymbol{B}_\parallel = B_\parallel \hat{\boldsymbol{e}}_z$ is the average magnetic field, parallel to the z-axis, and $\boldsymbol{B}_\perp$ is a perpendicular fluctuation. Throughout, we normalize the magnetic fields by $(\mu_0\rho)^{1/2}$, considering for the moment a medium with uniform density ρ_0 [$\boldsymbol{b}_\parallel = \boldsymbol{B}_\parallel/(\mu_0\rho)^{1/2}$ and $\boldsymbol{b}_\perp = \boldsymbol{B}_\perp/(\mu_0\rho)^{1/2}$]. The equations of RMHD become

$$\frac{\partial \boldsymbol{u}_\perp}{\partial t} + \boldsymbol{u}_\perp \cdot \nabla \boldsymbol{u}_\perp = -\nabla_\perp\left(\frac{p}{\rho_0} + \frac{1}{2}b_\perp^2\right) + \boldsymbol{b}_\perp \cdot \nabla \boldsymbol{b}_\perp + b_\parallel \frac{\partial \boldsymbol{b}_\perp}{\partial z} + \nu \nabla_\perp^2 \boldsymbol{u}_\perp, \qquad (1)$$

$$\frac{\partial \boldsymbol{b}_\perp}{\partial t} = \boldsymbol{b}_\perp \cdot \nabla \boldsymbol{u}_\perp - \boldsymbol{u}_\perp \cdot \nabla \boldsymbol{b}_\perp + b_\parallel \frac{\partial \boldsymbol{u}_\perp}{\partial z} + \eta \nabla_\perp^2 \boldsymbol{b}_\perp, \qquad (2)$$

$$\nabla \cdot \boldsymbol{u}_\perp = 0, \qquad \nabla \cdot \boldsymbol{b}_\perp = 0. \qquad (3)$$

As one can see from these equations, the nonlinear dynamics is confined to the planes perpendicular to the mean field $\boldsymbol{B}_\parallel$, while Alfvén waves propagate along the mean field. Direct simulations of these equations in one plane (Dmitruk et al. 1998; Georgoulis et al. 1998) and in a three-dimensional (3D) box (Dmitruk et al. 2003) have been carried out, but the Reynolds numbers obtained with such simulations are much too low to obtain a realistic inertial range of turbulence and long-term statistics. It is therefore our interest to simplify this model further by reducing the dynamics in the planes. This can be done by using shell models, as described below.

The plasma of the solar corona and solar wind is stratified, so one must allow for gradients of the mass density ρ even while considering incompressible couplings. Stratification couples incompressible Alfvén waves by introducing variations in Alfvén speed and, therefore, reflection (as well as amplification or depression of amplitudes due to the conservation of energy flux). Such terms may be written more clearly in terms of the Elsässer variables $\boldsymbol{Z}^\pm = \boldsymbol{u}_\perp \pm \boldsymbol{b}_\perp$ [with $\boldsymbol{b}_\perp = \boldsymbol{B}_\perp/(\mu_0\rho)^{1/2}$], in which case the effect of stratification on the linear propagation of modes may be written as

$$\frac{\partial \boldsymbol{Z}^\pm}{\partial t} \pm \boldsymbol{b}_\parallel \cdot \nabla \boldsymbol{Z}^\pm \mp \boldsymbol{Z}^\mp \cdot \nabla \boldsymbol{b}_\parallel \pm \frac{1}{2}(\boldsymbol{Z}^\mp - \boldsymbol{Z}^\pm)\nabla \cdot \boldsymbol{b}_\parallel = 0 \qquad (4)$$

(Velli 1993).

The first two terms describe the wave propagation, the third term describes the reflection of the waves by the perpendicular gradient of the Alfvén speed (which vanishes for a nondiverging flux tube), and the fourth term describes the growth or decrease in the normalized wave amplitude due to variations in Alfvén speed—ensuring conservation of wave energy flux—as well as the isotropic part of the reflection. We will incorporate these terms into the general framework of equations (1)–(3), but first we discuss how the nonlinear couplings are modeled in the shell approximation.

2.1. *Classical MHD Shell Models*

In shell models of incompressible MHD turbulence (Gloaguen et al. 1985; Biskamp 1994; Giuliani & Carbone 1998; Boffetta et al. 1999; Giuliani et al. 2002), one starts by taking the Fourier transform of the MHD equations and dividing wavevector space into concentric shells $S_n = \{\boldsymbol{k} \mid \|\boldsymbol{k}\| \in [k_n, k_{n+1}]\}$ with $k_n = k_0\lambda^n$, $n = 0, \ldots, n_\perp - 1$, and usually $\lambda = 2$. Also, a single complex scalar value u_n is chosen to represent the original longitudinal velocity increments $[\boldsymbol{u}(\boldsymbol{x} + \boldsymbol{\ell}) - \boldsymbol{u}(\boldsymbol{x})] \cdot \boldsymbol{\ell}/\ell$ on scales ℓ for $2\pi/\ell \in S_n$. The same approximation is made for the magnetic field: a scalar value b_n represents the magnetic field increments on the same scales ℓ. In this way the nonlinear interactions, originally a vector convolution in the 3D vector space, are reduced to a one-dimensional (1D) summation in terms of the shell index n. This one-dimensional model is the MHD analog of the Gledzer-Ohkitani-Yamada (GOY; Yamada & Ohkitani 1988) shell model of fluid turbulence.

One obtains the following equation, given by Giuliani & Carbone (1998):

$$\frac{dZ_n^\pm}{dt} = -k_n^2(\nu^+ Z_n^\pm + \nu^- Z_n^\mp) + ik_n T_n^{\pm *} + f_n^\pm, \qquad (5)$$

where $Z_n^\pm = u_n \pm b_n$ are the Elsässer-like variables, $\nu^\pm = (\nu \pm \eta)/2$ are combinations of kinematic viscosity and resistivity, $f_n^\pm$ are external driving forces, and $T_n^\pm$ is the nonlinear term, obtained by assuming (1) that the nonlinear interactions occur in triads of neighboring modes and (2) the conservation of the total pseudo-energies $E^\pm = \sum_n |Z_n^\pm|^2$ (and thus the energy $E = E^+ + E^-$ and the cross helicity $h_C = E^+ - E^-$) and a third invariant $H_K^\alpha = \sum_n \operatorname{sgn}(\delta - 1)^n k_n^\alpha |v_n|^2$, which depends on the dimensionality of the MHD system being modeled (Giuliani & Carbone 1998).

2.2. *Specifics of the Shell-Atm Model*

The "classical" GOY-like shell model that we have just presented corresponds to MHD, where the average magnetic field $\boldsymbol{B}_\parallel$ has not yet been separated out; in the Shell-Atm model we present now, the average magnetic field $\boldsymbol{B}_\parallel$ is separated out by starting from the RMHD equations (eqs. [1]–[3]). The new model we obtain corresponds basically to a pile of planes coupled by Alfvén waves, each containing a "classical" shell model for two-dimensional (2D) MHD (Fig. 1, *top*). This is similar to the loop model developed independently by Nigro et al. (2004), but the stratification of the atmosphere that we introduce allows to use this model in a large variety of cases of coronal loops or other structures (although we do not use this specific feature in the runs presented in this paper). The Shell-Atm model has the following properties:

1. The profile of the Alfvén speed $b_\parallel(z)$ along the mean field (i.e., the atmospheric structuring of the plasma) is given through a density stratification $\rho_0(z)$, an areal expansion factor of the flux tube $A(z)$, and magnetic flux conservation. The latter two effects imply that the width of the loop and corresponding wavenumber k_0 must also, in general, depend on z.
2. The Elsässer variables $Z_n^\pm$ now depend on the position z of the plane along the main axis of the simulation box, and the left-hand

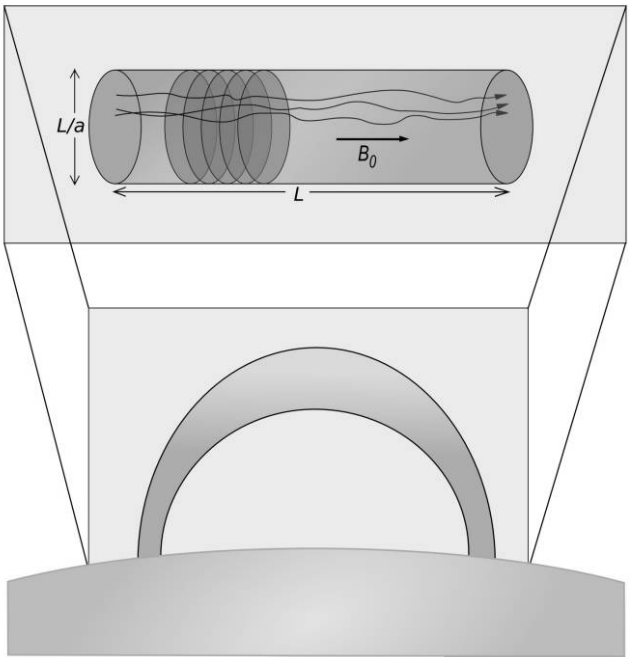

FIG. 1.—*Top*: Layout of the Shell-Atm model in the general case; shell models in planes orthogonal to $\boldsymbol{B}_\parallel$ are piled up along $\boldsymbol{B}_\parallel$. *Bottom*: In the case of a coronal loop, the loop is unbent into the cylindrical simulation box.

side of equation (5) is replaced by the term $(\partial_t \pm b_\parallel \partial_z)Z_n^\pm \pm \frac{1}{4}Z_n^\pm \partial_z(\ln \rho) \pm \frac{1}{2}Z_n^\mp \partial_z b_\parallel$, corresponding to linear Alfvén wave propagation in a stratified static atmosphere (eq. [4]). As a result, the external driving forces $f_n^\pm$ are not needed anymore, as energy can simply be input as an incoming energy flux at the boundaries.

3. The nonlinear interactions occur inside each plane, in two dimensions. In this case the third invariant of MHD is anastrophy, that is, the total square modulus of the magnetic potential (H_K^α with $\alpha = 2$). The coefficients of the nonlinear terms $T_n^\pm$ of the shell model are then those of Giuliani & Carbone (1998) with parameters $\alpha = 2$ and $\delta > 1$ (i.e., $\delta = 5/4$ and $\delta_m = -1/3$).

To summarize, the fields of the Shell-Atm model are the complex variables $Z_n^\pm(z, t)$, which are the Elsässer-like fields $u_n(z, t) \pm b_n(z, t)$. Here n is the index of the shell, corresponding to the perpendicular wavenumber $k_n(z) = k_0(z)\lambda^n$, with $\lambda = 2$; it can be any integer (positive or negative), but for numerical computations it is convenient to assume that $Z_n^\pm(z, t)$ is zero outside some domain $[0, n_\perp - 1]$.[4] The quantity z is the position on the axis supporting $\boldsymbol{B}_\parallel$, in a domain $[0, L]$ discretized over n_z planes. The equations of the model are

$$\begin{aligned}(\partial_t \pm b_\parallel \partial_z)Z_n^\pm \pm \tfrac{1}{4}Z_n^\pm \partial_z(\ln \rho) \pm \tfrac{1}{2}Z_n^\mp \partial_z b_\parallel \\ = -k_n^2(\nu^+ Z_n^\pm + \nu^- Z_n^\mp) + ik_n T_n^{\pm *}\end{aligned} \qquad (6)$$

with $T_n^\pm$ given by Giuliani & Carbone (1998) (with $\alpha = 2$, $\delta = 5/4$, and $\delta_m = -1/3$).

2.3. *Quantities Derived from the Fields of the Model*

As $Z_n^\pm(z, t)$ represents the Elsässer field at perpendicular wavenumbers included in the shell S_n and at position z, $|Z_n^\pm(z, t)|^2/4$ is the energy per unit mass at position z at time t in the modes included in shell S_n. If we assume that the modeled loop is a cylinder of diameter $2\pi/k_0$ and that, after discretization in the z-direction, the separation between planes (i.e., the thickness of each plane) is δz, then the cross section of the loop by a plane is $A = \pi^3/k_0^2$ and the volume associated with each plane is $V = A\ \delta z$; with a mass density ρ_0, the mass associated with each plane is $m = \rho_0 A\ \delta z$ and the energy contained in the field $Z_n^\pm(z, t)$ is

$$E_n^\pm(z, t) = \frac{m}{4}|Z_n^\pm(z, t)|^2 = \frac{\rho_0}{4}\frac{\pi^3}{k_0^2}\delta z |Z_n^\pm(z, t)|^2. \qquad (7)$$

E_n as a function of n (for any field, position, and time) will hereafter be referred to as the "shell energy spectrum." To obtain a 1D perpendicular spectrum (as those given by turbulence theories), we need in addition to take into account the geometry of the shell S_n in Fourier space: for a shell model representing 2D MHD, S_n has an area $\mathcal{S}(S_n) = \pi k_n^2(\lambda^2 - 1)$. It follows that the 2D energy spectral density in the shell is $E_n/\mathcal{S}(S_n)$ and that the 1D energy spectral density is $2E_n/[k_n(\lambda^2 - 1)]$. Note that for this reason there is a difference of 1 between the slope of a power-law 1D perpendicular spectrum (e.g., $-5/3$ for a spectrum as in Kolmogorov 1941) and the slope of its "shell energy spectrum" counterpart (e.g., $-2/3$).

2.4. *Scales of Quantities of the Model and Timescales*

The equations are rendered nondimensional by introducing characteristic units of time, length, and density. For the coronal situation we choose 10^7 m for the unit of length, 1 s for the unit of time, and 10^9 kg for the unit of mass. Then the units of the other quantities derive naturally from these basic units and are 10 Mm s^{-1} for velocity, 10^{-12} kg m^{-3} for mass density, 10^{14} m^2 s^{-1} for diffusivities, 10^{23} J for energies, and 10^{23} W for powers.

The characteristic timescales for each of the terms of equation (6) are deduced from their orders of magnitude:

$$\partial_t Z \sim b_\parallel \frac{k_\parallel}{2\pi} Z \sim \bar{\nu} k_\perp^2 Z \sim k_\perp Z^2, \qquad (8)$$

where Z is the order of magnitude of the fields $Z_n^\pm$ of the model at wavenumbers $k_\parallel$ (parallel to $\boldsymbol{B}_\parallel$) and $k_\perp = k_0\lambda^n$, and where $\bar{\nu}$ represents either ν or η. We obtain

1. The Alfvén time, $\tau_A = 2\pi/(b_\parallel k_\parallel)$;
2. The characteristic time of dissipation, $\tau_\nu = (\bar{\nu} k_\perp^2)^{-1}$;
3. The characteristic time of nonlinear interactions $\tau_{NL} = [k_\perp Z(k_\perp)]^{-1}$ in the planes; and
4. The wave reflection timescale, $t_R = 2/\partial_z b_\parallel$.

The maximum Alfvén time $\tau_{A,\max}$ is obtained for $k_\parallel = 2\pi/L$ and corresponds to the time needed by the wave to cross the simulation box. By taking, on the other hand, the minimum of all the characteristic times in the box [using $k_\parallel = 2\pi/\delta z$ to get $\tau_{A,\min}$, $k_\perp = k_{n_\perp - 1}$ to get $\tau_{\nu,\min}$, and $\tau_{NL,\min} = ([k_\perp Z(k_\perp)]_{\max})^{-1}$], we can estimate the time step needed by a numerical scheme according to the Courant-Friedrichs-Lewy (CFL) condition.

Other timescales also appear in the Shell-Atm model:

1. The correlation time t^* of the forcing, which depends on the precise form of the forcing (see § 2.5 for the case of a coronal loop); and
2. The turbulent cascade timescale $\tau_{\text{cascade}} = \sum_n \tau_{NL}(k_\perp = k_n)$, where the sum is taken over the modes n of the inertial range of the spectrum (see § 3.2).

2.5. *Case of a Coronal Loop*

Geometry.—For the case of coronal loops forced by photospheric motions, we consider the loops to be "straightened out" as seen in Figure 1 (*bottom*). This is similar to the cellular automaton model presented in Buchlin et al. (2003), but here the nonlinear interactions between modes of MHD turbulence are represented through shell models instead of cellular automata. Furthermore, for simplicity we choose uniform density ρ_0, Alfvén speed $b_\parallel$, and loop width $(2\pi/k_0)$; more realistic cases will be studied in future work.

---

[4] The energy flux from the domain $[0, n_\perp - 1]$ outward is then zero, as can easily be seen using the equation of the spectral energy flux (eq. [14]) for $n = 0$ and $n = n_\perp$.

Forcing.—With this geometry, the boundary planes of the model represent the footpoints of the loop, which are anchored in the photosphere. We choose to impose a time-dependent vortex-like velocity field on the modes at larger scales, corresponding to photospheric convective motions at the scale of the supergranulation. Since the velocity is imposed, waves traveling along the loop are partially reflected at the photosphere.

The imposed velocity field $u_n(z, t)$ on each mode n of both boundary planes $z = 0$ and $z = L$ has the form

$$u_{z,n}(t) = u_{f,n}[e^{2i\pi A_{z,n}} \sin^2(\pi t/t^*) + e^{2i\pi B_{z,n}} \sin^2(\pi t/t^* + \pi/2)], \qquad (9)$$

where $u_{f,n}$ is the amplitude of the forcing (nonzero only for some n corresponding to scales $2\pi/k_n$ of the supergranulation) and $A_{z,n}$ and $B_{z,n}$ are independent random complex coefficients of modulus 1 whose complex arguments are uniformly distributed over $[0, 2\pi]$. These coefficients are kept constant during time intervals of duration t^*, and they are randomly changed when $t \equiv 0 \pmod{t^*}$ and $t \equiv t^*/2 \pmod{t^*}$ respectively, that is, when the corresponding $\sin^2$ term is zero. This is another difference from the model of Nigro et al. (2004), who force by using a stochastic velocity function on one boundary plane only. The autocorrelation time of the forcing field is then on the order of t^*, which is chosen to be much longer than all the other timescales of the model (§ 2.4).

In practice, this boundary condition is realized by imposing an incoming Alfvén wave $Z_n^+(0, t) = -Z_n^-(0, t) + 2u_{0,n}(t)$ at the boundary $z = 0$ and an incoming Alfvén wave $Z_n^-(L, t) = -Z_n^+(L, t) + 2u_{L,n}(t)$ at the boundary $z = L$. The resulting power entering the loop is

$$\epsilon_f = \frac{1}{4}\sum_n \rho_0(0) b_\parallel(0) A(0)[|Z_n^+(0,t)|^2 - |Z_n^-(0,t)|^2] + \frac{1}{4}\sum_n \rho_0(L) b_\parallel(L) A(L)[|Z_n^-(L,t)|^2 - |Z_n^+(L,t)|^2]. \qquad (10)$$

Note that this power is not imposed but depends on the fields already contained in the simulation box.

3. NUMERICAL SIMULATIONS AND ANALYSIS OF THE RESULTS

3.1. *Energy*

3.1.1. *Energy Balance*

Alfvén wave propagation, as well as the nonlinear terms in our shell model, conserves energy, so that changes in the total energy in the loop arise only from flux through the photospheric boundaries (i.e., the forcing) and from the dissipation. This energy balance is well verified in practice, within 1% in general as can be seen in Figure 2, as long as the numerical dissipation due to the numerical scheme for wave propagation is not too high; the condition for this is that the perpendicular dissipation scales not be too small compared with the separation between planes in the z-direction.

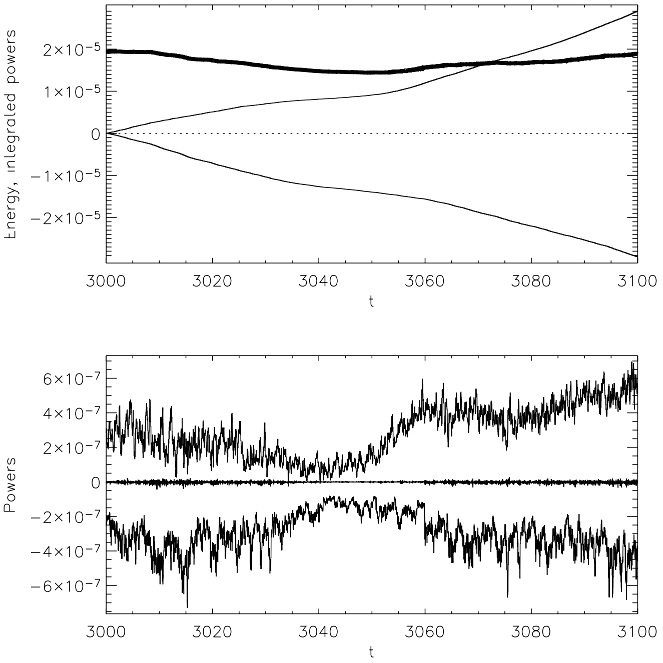

FIG. 2.—Energy balance in the model. *Top*: Energies and integrated dissipation powers (*upper thin line*, integrated power of forcing; *lower thin line*, integrated dissipation power; *thick line*, energy, and sum of integrated contributions of powers). The small deviation (only 1% over the time span of this plot) of the energy compared with the sum of integrated powers shows that the numerical dissipation is low. *Bottom*: Power time series (*top to bottom*, forcing power, numerical dissipation power, and dissipation power). Quantities with negative contributions to the energy balance are shown as having negative values. [*See the electronic edition of the Journal for a color version of this figure.*]

3.1.2. *Ratio of Magnetic to Kinetic Energy*

The ratio of the magnetic to kinetic energy in the stationary state may be estimated as follows: First, a simple linear estimate of the velocity field leads to

$$\boldsymbol{u}_\perp = \boldsymbol{u}_{\perp,0}(x,y)\cos(\omega_{\rm ph} t)\, z/L, \qquad (11)$$

where $\omega_{\rm ph}/2\pi$ is the characteristic frequency of the photospheric motions, while the magnetic field is given by

$$\boldsymbol{b}_\perp = \boldsymbol{u}_{\perp,0}(x,y) b_\parallel t/L. \qquad (12)$$

The relative importance of the higher frequency modes to this low-frequency energy flux was discussed by Milano et al. (1997); given that the Alfvén wave travel time along a loop is on the order of seconds, while most of the power in photospheric motions is in the minutes-to-hour range, it is the low-frequency resonance that plays the more important role. Energy injection from the photosphere into the corona therefore grows as t^2 and is stored in the transverse coronal magnetic field, while the velocity field is bounded by its photospheric value. The linear solution will eventually break down, because the magnetic field determined by equation (12) is not in general force-free and therefore will cause the coronal field to evolve dynamically. The ratio of magnetic to kinetic energies at this point may be estimated dimensionally by asking for the change in coronal velocity field determined by nonlinear interactions in equation (1) to be of the same order of magnitude as the field given by equation (11). Denoting the rms photospheric speed by u_f, after a time Δt the nonlinear term has the dimensional value $u_f^2 b_\parallel^2 \Delta t^2/lL^2$, growing quadratically with time. It will cause a change in the coronal loop velocity field

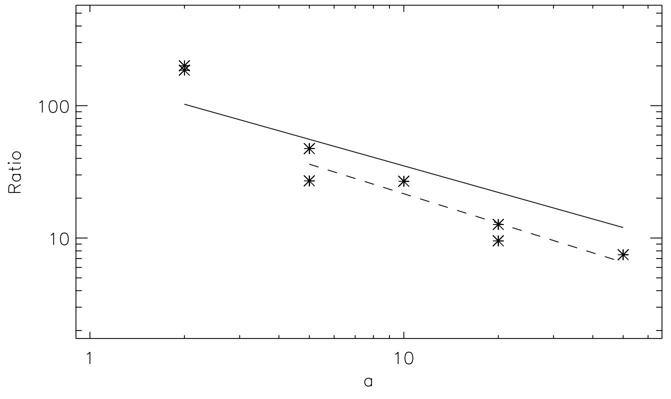

FIG. 3.—Ratio of average magnetic to kinetic energy as a function of aspect ratio, plotted with the theoretical scaling (*solid line*) derived from eq. (13) and a power-law fit (*dashed line*; slope -0.74 ± 0.14), for parameters $b_\parallel = 1$, $l = 0.1$, and $u_{f,n} = 10^{-3}$.

of the same order as u_f over the time Δt, when $u_f^2 b_\parallel^2 \Delta t^2/lL^2 \sim u_f/\Delta t$. One then recovers the time Δt as $\Delta t \sim \tau_{\rm A,\,max}^{2/3}\tau_e^{1/3}$, where $\tau_{\rm A,\,max}$ is the loop crossing time while $\tau_e = l/u_f$ is the nonlinear time calculated on the photospheric velocity. The ratio of magnetic to kinetic energies in the corona at this stage is then

$$\frac{E_b}{E_u} = 3\left(\frac{\Delta t}{\tau_{\rm A,\,max}}\right)^2 = 3\left(\frac{\tau_e}{\tau_{\rm A,\,max}}\right)^{2/3}, \qquad (13)$$

which we associate with the saturation level of magnetic to kinetic energy. This ratio should be a function of the aspect ratio $a = b_\parallel \tau_{\rm A,\,max}/l$ of the loop. To check whether the Shell-Atm model follows this dependence, we perform a series of simulations with parameters $b_\parallel = 1$, $k_0 = 20\pi$ (i.e., a width $l = 0.1$), $\nu = \eta = 10^{-9}$, and $u_{f,n} = 10^{-3}$ for $n \in [2, 4]$. The number of shells is $n_\perp = 16$, and the number of planes n_z is taken in the set $\{200, 500, 1000, 2000, 5000\}$ with a separation 10^{-3} between planes in all cases, leading to lengths $L \in \{0.2, 0.5, 1, 2, 5\}$ and aspect ratios $a \in \{2, 5, 10, 20, 50\}$.

The ratio of magnetic energy to kinetic energy in the stationary state is plotted as a function of aspect ratio in Figure 3, together with what is expected from equation (13). The numerical results we obtain roughly support this scaling, although the experimental ratios are smaller than the theoretical ratios by a factor of 1.36, and the values for an aspect ratio $a = 2$ deviate from the scaling obtained for other aspect ratios. The slight departure from the proposed scaling, and the fact that the saturation level of magnetic to kinetic energy is lower than predicted, could be due to the "leakage" of energy to the higher frequency resonances of the loop (as shown in Fig. 13 below).

3.2. *Spectra*

3.2.1. *Formation of the Spectra and Spectral Energy Flux*

The energy flux in each plane from the shells $k < k_n$ to the shells $k \geq k_n$ is the derivative of the energy contained in the shells $k \geq k_n$ due to the nonlinear terms $T_n^\pm$, namely,

$$\begin{aligned}\Pi_n = -\frac{k_n}{4\lambda^2}\Im \sum_{s=\pm1} & (\delta_m - \delta)Z_{n-2}^{-s}Z_{n-1}^{s}Z_n^{s} \\ & + (2 - \delta - \delta_m)Z_{n-2}^{s}Z_{n-1}^{-s}Z_n^{s} \\ & + \lambda[(\delta + \delta_m)Z_{n-1}^{s}Z_n^{s}Z_{n+1}^{-s} \\ & + (2 - \delta - \delta_m)Z_{n-1}^{s}Z_n^{-s}Z_{n+1}^{s}]. \qquad (14)\end{aligned}$$

With $b_n = 0$, we recover the hydrodynamic spectral energy flux given in equation (2) of Frick & Sokoloff (1998). Furthermore, this energy flux is consistent with the general idea that the energy flows "downhill" in the 1D perpendicular energy spectrum.

When starting the simulation from a very low amplitude field (Fig. 4), the magnetic energy and then the kinetic energy at the scales of the forcing grow, and when the fields are sufficiently large, nonlinear effects become visible as energy is transferred to modes beyond those initially forced. In particular, there is a flux to higher $k_\perp$ mode numbers ($\Pi_n > 0$, direct cascade), which continues to the highest wavenumbers where dissipation occurs, as well as a flux to smaller wavenumbers ($\Pi_n < 0$, inverse cascade), which energizes modes at the largest scales and saturates at a level comparable to the forced modes.

As a result of the energy cascade, an inertial range appears between the forcing and the dissipation scales, in the same way as in the original shell models. The energy flux Π_n across shells is uniform on average over the whole inertial range. The Reynolds number in the case shown here can be evaluated to 10^6, which is much higher than any Reynolds number from direct numerical simulations. Even higher Reynolds numbers can be attained by using more shells and planes, at the cost of the ability to do long-term statistics.

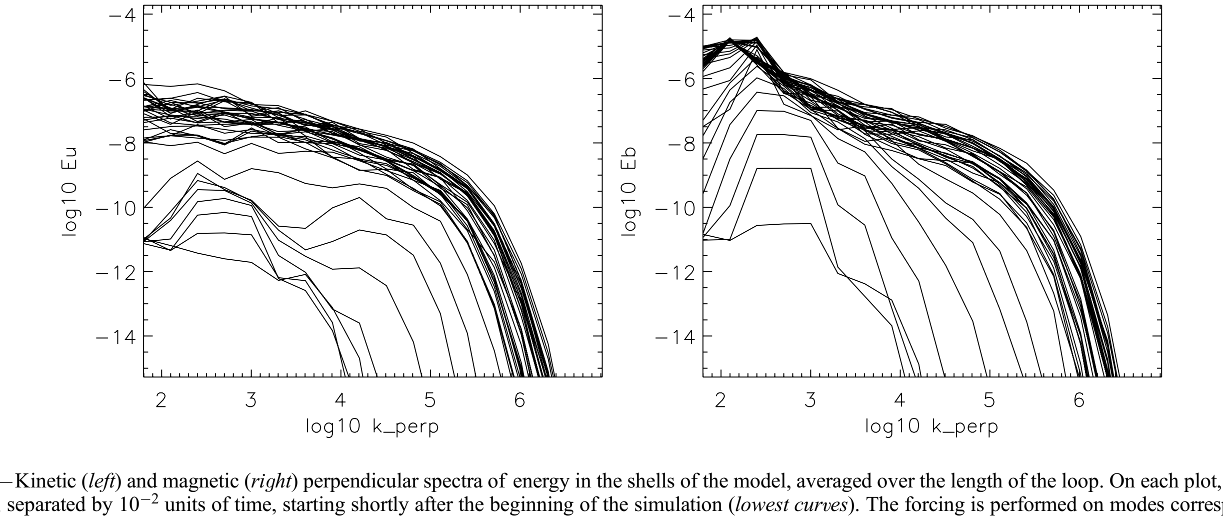

FIG. 4.—Kinetic (*left*) and magnetic (*right*) perpendicular spectra of energy in the shells of the model, averaged over the length of the loop. On each plot, 40 spectra are shown, separated by 10^{-2} units of time, starting shortly after the beginning of the simulation (*lowest curves*). The forcing is performed on modes corresponding to $\log k_n = 2.4$–3.0.

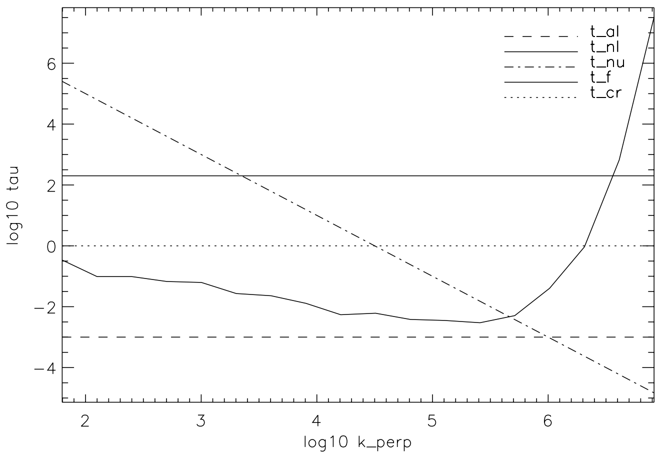

FIG. 5.—Timescales as a function of $k_\perp$: Alfvén time $\tau_{\mathrm{A,min}}$, nonlinear time τ_{NL}, dissipation time τ_ν, forcing correlation time t^*, and crossing time $\tau_{\mathrm{A,max}}$ (*top to bottom in the figure key*).

3.2.2. *Fluctuations of the Spectra*

Once in the stationary phase, the spectra continue to fluctuate, with characteristic timescales linked to the "local" timescales—that is, the timescales, as described in § 2.4, considered as depending on the mode k_n (Fig. 5). The most relevant timescale seems to be the local nonlinear timescale $\tau_{\mathrm{NL}}(k)$, defined in § 2.4, as this is the timescale on which the energy in a given mode n can change under the action of the nonlinear terms in equation (6). More precisely, no dynamics occurs at timescales below the local nonlinear timescale, as can be seen in Figure 6: the modes with low $k_\perp$ thus only have long fluctuation times, excited by the long timescales of the forcing, while the modes with high $k_\perp$ fluctuate quickly, but still with long characteristic times due to the flow of energy coming from the modes at low $k_\perp$ (these long-term fluctuations are common to the whole spectrum).

3.2.3. *Evolution of the Spectra during an Event*

To understand what happens during episodes of high energy dissipation, we have analyzed the spectra of the fields before, during, and after such an episode. The differences in spectra with respect to an average spectrum (Fig. 7) show that before the event (maximum dissipation corresponds to the red spectrum differences), the energy accumulates over the whole spectrum. The total energy is then high, the nonlinear times are short, and energy flows rapidly down to the smallest scales according to equation (14): it enhances the spectra at the largest wavenumbers by several orders of magnitude, leading to a strong enhancement of the dissipation power. As energy is released, this process then leads to a decrease of the spectrum, first in the dissipative range (high wavenumbers) and then in the whole spectrum. The dissipation power is then low again, and as the nonlinear timescales in the inertial range are longer, the energy injected at the largest scales cannot flow to the smallest scales as fast as before: the energy does not easily reach the dissipative scales, and the dissipation power remains low until the next such episode.

Nigro et al. (2005) underline that the leading term of the energy flux across scales (eq. [14]) is proportional to $k_n b_n^2 u_n$ (with the notations of the shell-model variables), and they also observe short-term variations of the kinetic energy spectrum around a dissipation event. These variations appear to control the energy flux to the smallest scales and, then, the dissipation. In addition, we have shown that these variations exist on a longer term around an event, and that the magnetic energy spectrum also varies on the same timescales. The cross-scale energy flux may thus be controlled by both the kinetic and the magnetic energy spectra.

3.2.4. *Slopes of the Spectra*

The slopes of the power-law 1D perpendicular spectra of the velocity and magnetic field (Fig. 4) seem to be roughly equal in the inertial range, but as the spectra fluctuate with time, there are fluctuations of the slopes. The distribution of these slopes obtained at different times is shown in Figure 8: the median slope is -1.89 (with standard deviation 0.10) for the velocity spectrum and -1.81 (with standard deviation 0.13) for the magnetic spectrum. It appears that, on average, the kinetic spectrum is slightly steeper (by 4%) than the magnetic spectrum. If we look specifically at the times when the total dissipation power exceeds its 90th percentile, that is, during events of energy dissipation, the spectra are slightly shallower, with the median slopes being -1.83 and -1.77 for the velocity and magnetic spectra, respectively. This reflects the fact that more energy is present at small scales during events of energy dissipation (Fig. 7, *red curves*).

These 1D spectra are different from those found by Nigro et al. (2005) corresponding to 1D spectra of slope $-5/3$ for velocity and approximately -3 for magnetic field; an explanation could be that their inertial range was smaller, and that their fitting range includes scales where forcing occurs.

3.2.5. *Parallel and Perpendicular Spectra*

In this model, nonlinear interactions occur only in perpendicular planes. Development of small scales along the magnetic field is thus merely a consequence of the Alfvénic propagation of differences in the dynamics in different planes. One therefore expects parallel and perpendicular spectra to be different, with a relationship determined by the so-called critical-balance condition, namely, that for a given perpendicular scale, differences in the parallel direction can appear only between planes such that the Alfvén propagation time is longer than the (perpendicular) nonlinear time at that same scale (see, e.g., Goldreich & Sridhar 1995; Cho et al. 2002; Oughton et al. 2004). In the present model, assuming a $k^{-\alpha}$ 1D energy spectrum (i.e., a $k^{-\alpha+1}$ "shell energy spectrum"), the nonlinear timescale is $\tau_{\mathrm{NL}}(k_\perp) \propto k^{(\alpha-3)/2}$. With a constant and uniform advection velocity $b_\parallel$, the critical-balance condition can be expressed as

$$k_\parallel \lesssim \frac{Z(k_0)}{b_\parallel} k_\perp^{(3-\alpha)/2} k_0^{(1-\alpha)/2}. \tag{15}$$

Note that with a Kolmogorov $\alpha = 5/3$ spectrum, we recover the result $k_\parallel \propto k_\perp^{2/3}$ of Goldreich & Sridhar (1995).

For a field $a_n(z)$ of the model at a given time t (a can be $Z_n^\pm$, u_n, or b_n), let $\tilde{a}_n(k_\parallel)$ be its Fourier transform along the z-axis. We obtain the two-dimensional power spectrum of a (a function of $k_\perp = k_n$ and $k_\parallel$) from

$$\mathcal{A}(k_\perp, k_\parallel) = \frac{c}{k_n} \left|\tilde{a}_n(k_\parallel)\right|^2, \tag{16}$$

where c is a constant.

To obtain a sufficient wavenumber range in the parallel and perpendicular directions, we need to perform simulations with a very large number of planes. This is achieved by starting a simulation with a number of planes $n_{z,0}$ and then, once the energy has reached its final order of magnitude, by stopping the simulation and resuming it after having interpolated the fields in the z-direction. We can perform several iterations of this process if

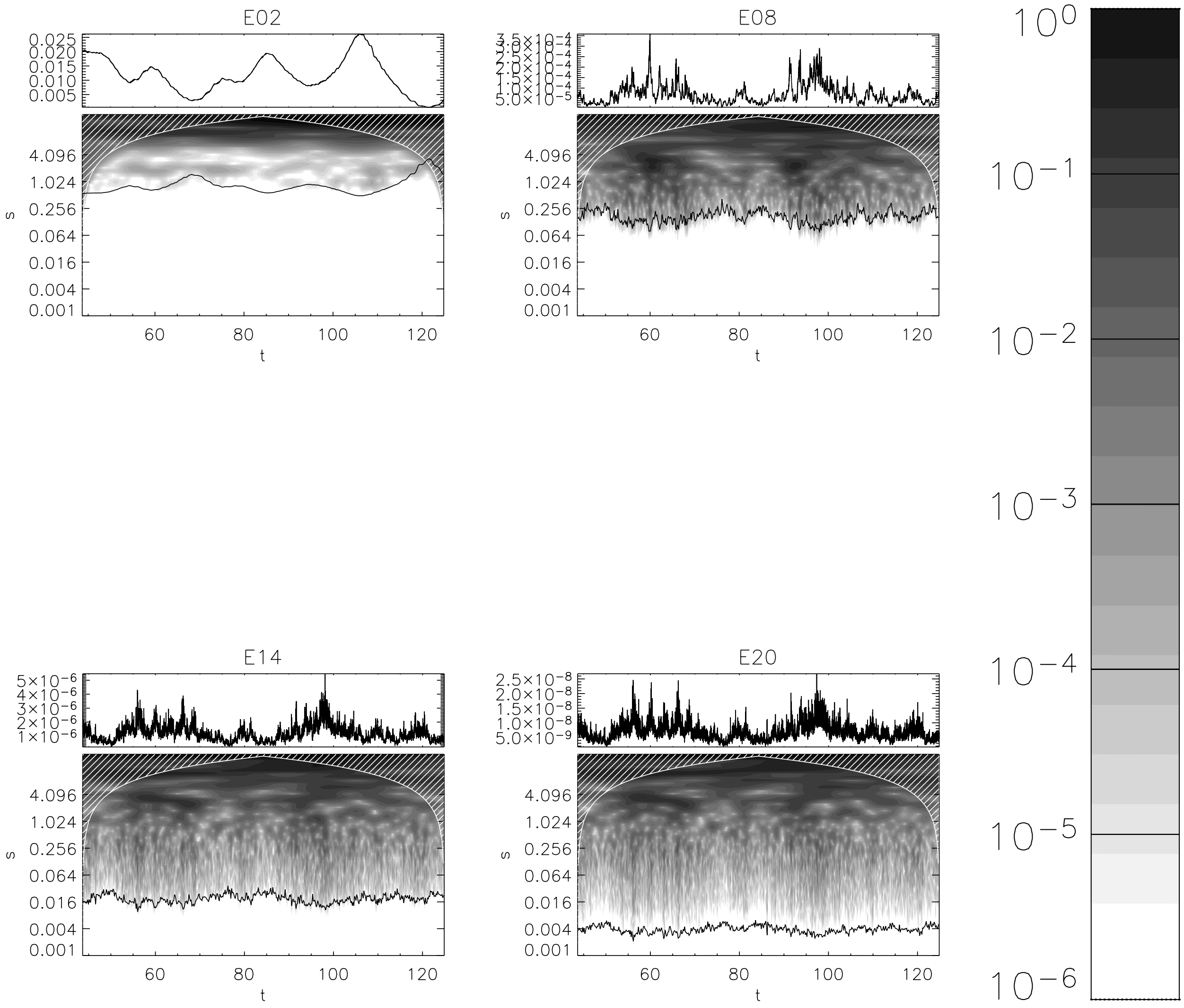

FIG. 6.—Time series of the total energy contained in the shells $n \in \{2, 8, 14, 20\}$ of the model, and Morlet wavelet timescale planes of each of these time series. The axes of the timescale planes are time (horizontally) and timescale (vertically, logarithmic). The theoretical nonlinear timescale $\tau_{\rm NL}(k_n)$ as a function of time has been superposed on each timescale plane. [*See the electronic edition of the Journal for a color version of this figure.*]

needed. Figure 9 shows a 2D spectrum obtained by summing the Z^+ and Z^- spectra and averaging them over 10 times separated by $10\tau_{\rm A,\,max}$, during a run with $n_z = 10n_{z,0} = 5000$ planes (runs with 50,000 planes were also performed). The level lines in $(k_\perp, k_\parallel)$-space are clearly noncircular and appear to follow the critical-balance ellipses (eq. [15]) at large $k_\perp$, although with an excess of energy in the parallel direction. The anisotropy angle as defined by equation (5) of Del Zanna et al. (2001) computed in the range $\log k \in [1.8, 4.4]$ (where the spectrum is known as a function of both $k_\perp$ and $k_\parallel$) is 67°, which confirms that the spectrum is elongated in the perpendicular direction.

3.3. *Dissipation, Heating Function, and Statistical Properties*

Heating function.—If we look at the energy dissipation power per unit length as a function of both time and position along the loop, we get the "heating function" (Fig. 10*a*). We see again (and for the same reasons as before) short-lived events of dissipation, and they correspond to short structures along the axis of the loop, whose size is on the order of the propagation distance of the structure during its lifetime. Some Alfvén wave packets are also strong enough to be dissipated only after interacting with many counterpropagating wave packets, and thus they live longer and leave an oblique trace in the heating function during their propagation.

Furthermore, when we look at the heating function at long timescales, of hundreds of crossing times $\tau_{\rm A,\,max}$ (Fig. 10*b*), some features appear that are related to the slow variations of the total energy (mainly contained in the slowly varying low-$k_\perp$ modes) under the effect of the slow forcing, of timescale t^* (which is chosen to be a few hundred $\tau_{\rm A,\,max}$). The time variations of the dissipation power at these timescales (corresponding to a few minutes of physical time) seem to be almost the same at all positions along the loop. This is consistent with the common statement that the loops are heated as a whole, even though (1) the elementary events of dissipation, as seen in Figure 10*a*, are each small compared with the length of the loop and (2) thermodynamics, which would further smooth out the appearance of the heating function obtained from observable variables (because of the fast conduction times), has not yet been taken into account.

Dissipation power time series.—The integral of the heating function along the loop is the time series of the power of energy dissipation $\epsilon(t)$, shown in the lower portions of Figures 10*a*–10*b*. These time series display spikes of high dissipation power at short timescales during high-activity periods, as is usually found in both

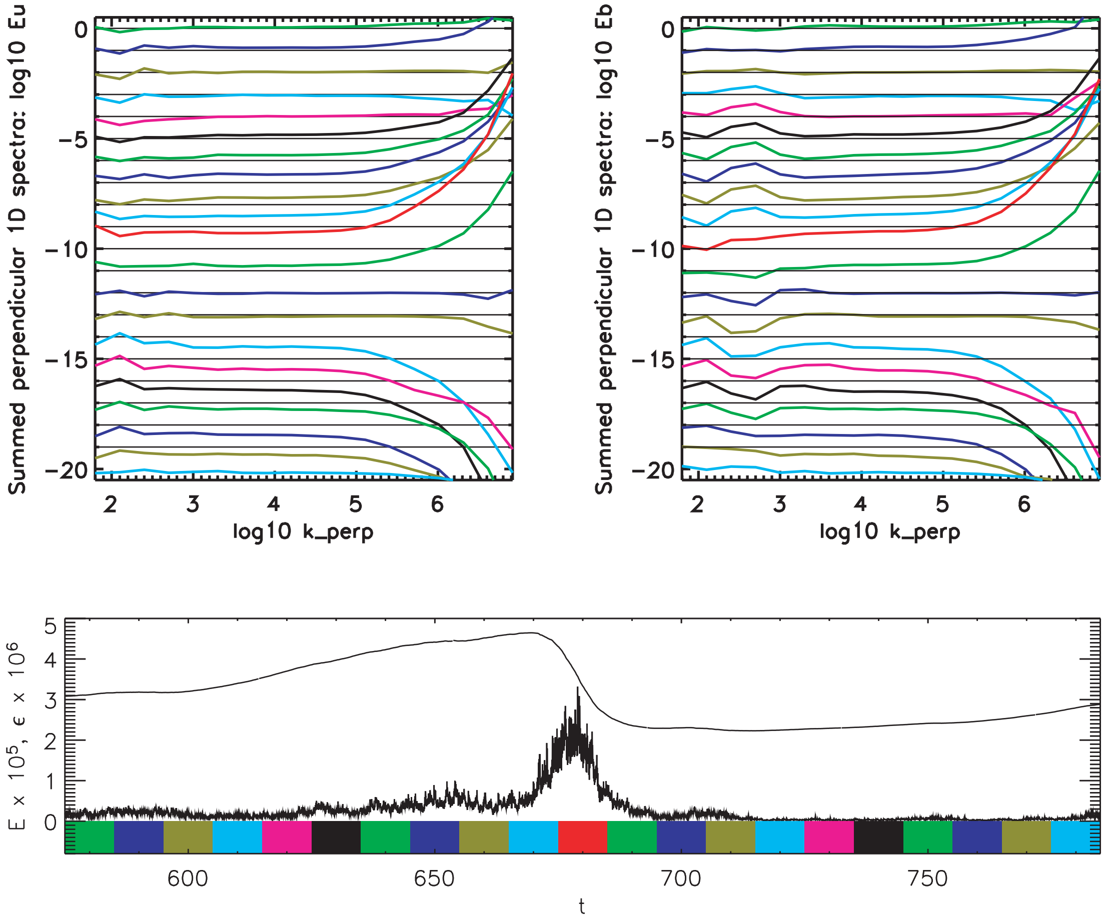

FIG. 7.—*Top left*: Differences between kinetic perpendicular spectra of energy in the shells of the model and their average (in logarithmic space). The spectra are averaged over the length of the loop and are plotted at times surrounding an event of dissipation power (corresponding to the red spectra): 10 spectra are shown before the event, and 10 spectra are shown after; the difference spectra are each separated by 10 units of time, and are stacked from top to bottom, with a shift of 1 unit of the y-axis between each. *Top right*: Same plot for the magnetic energy spectra. *Bottom*: Time series of energy and dissipation power, with the colors corresponding to the time intervals used to compute the spectra.

observations of solar flares and simulations of high Reynolds number MHD turbulence. The dissipation time series are analyzed further below.

Average profile of dissipation power.—On the other hand, the time average of the heating function, that is, the average power of energy dissipation per unit length as a function of position along the loop, shown in Figure 10*c*, is almost flat and drops only near the loop footpoints. This would suggest that coronal heating takes place almost uniformly along loops, although not at footpoints; however, one must bear in mind that these simulations do not yet take into account realistic profiles of density and magnetic field.

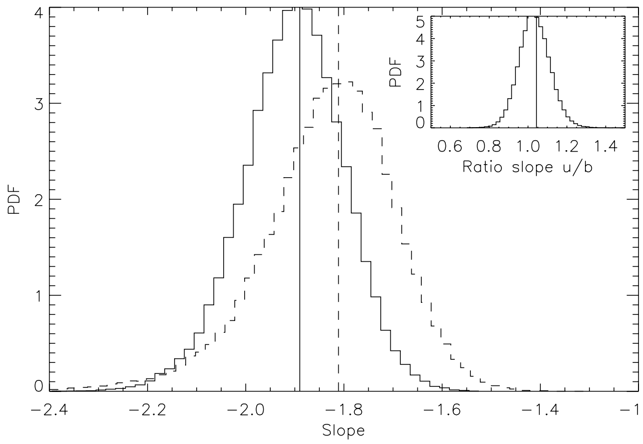

FIG. 8.—Distribution function of the slopes of the 1D perpendicular spectrum averaged along $\boldsymbol{B}_\parallel$, for the kinetic (*solid line*) and magnetic (*dashed line*) fields. The median slopes are respectively −1.89 and −1.81 and are plotted as vertical lines. The distribution of the ratios between the slopes for kinetic and magnetic perpendicular spectra is shown in the inset, together with its median value of 1.044.

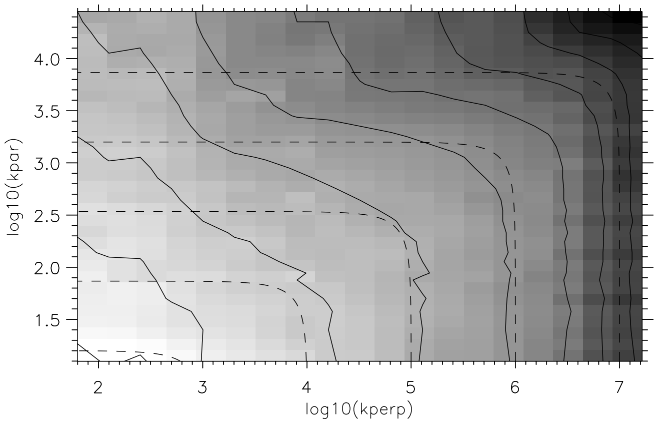

FIG. 9.—Total spectrum of the Z^+ and Z^- fields, as a function of the perpendicular and the parallel wavenumbers. The solid lines are level lines, and the dashed lines are ellipses with axes $k_\perp$ and $k_\parallel \propto k_\perp^{2/3}$, for different values of $k_\perp$.

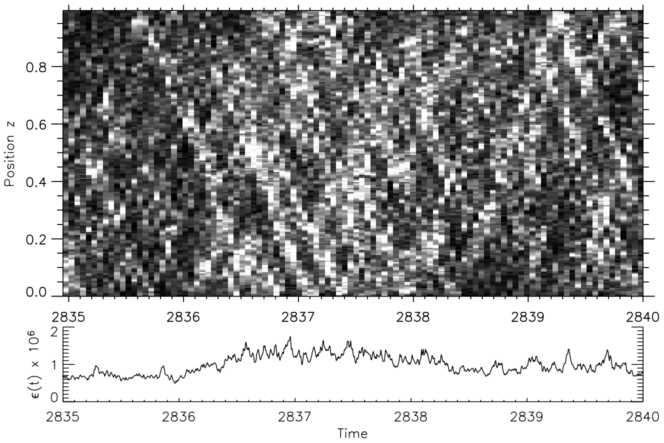

FIG. 10*a*

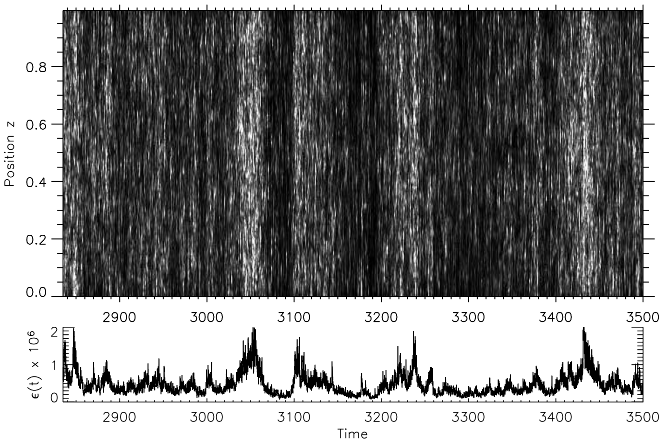

FIG. 10*b*

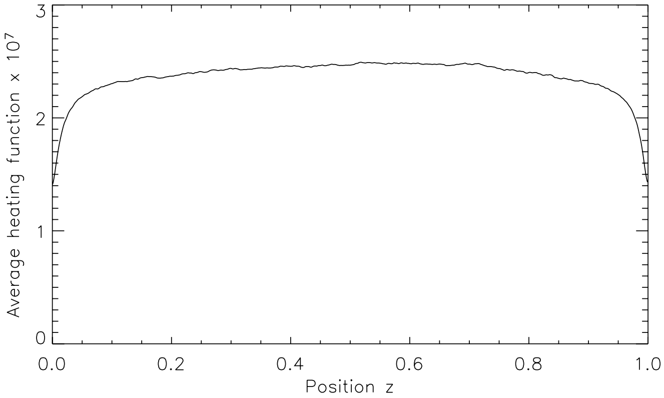

FIG. 10*c*

FIG. 10.—(*a*, *b*) Heating function, or power of energy dissipation per unit length, as a function of time *t* and position *z* along the loop. Two different time intervals are shown. The lower plot in each panel represents the integral along the loop of the heating function (i.e., the total power of energy dissipation as a function of time). (*c*) Time average, over $1200\tau_{\mathrm{A,max}}$ following (*a*), of the heating function as a function of position along the loop.

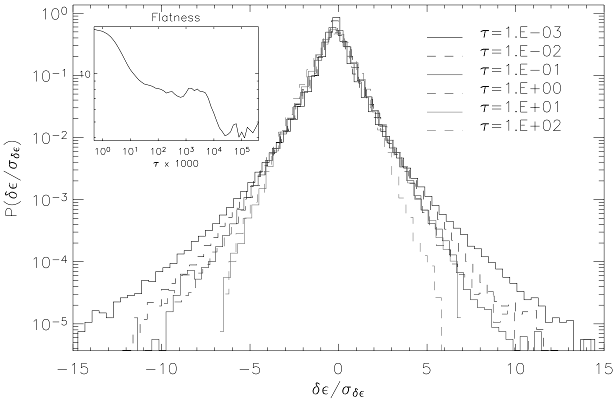

FIG. 11.—Distributions of the increments of the energy dissipation power time series for different time lags. *Inset*: Flatness corresponding to these dissipation power increments. [*See the electronic edition of the Journal for a color version of this figure.*]

Intermittency.—The increments $\delta_\tau\epsilon(t) = \epsilon(t+\tau) - \epsilon(t)$ of the time series $\epsilon(t)$ at a given time lag τ have a distribution whose shape depends on the lag: in Figure 11, the distributions of the $\delta_\tau\epsilon(t)$ normalized by their standard deviation have wider wings for short time lags than they do for long time lags. Hence the time series is intermittent, which is confirmed by the rise of the flatness (fourth normalized structure function) $F(\tau) = \langle|\delta_\tau\epsilon(t)|^4\rangle_t/\langle|\delta_\tau\epsilon(t)|^2\rangle_t^2$ for small time lags τ (Fig. 11, *inset*). This intermittency is a consequence of the intermittency that can be observed in the velocity and magnetic fields of the model and is also predicted by models such as those of She & Leveque (1994) in hydrodynamics and Politano & Pouquet (1995) in MHD. It could be a consequence of the fluctuations of the spectral flux resulting from the long-term global fluctuations of the spectrum, which have been seen in § 3.2.2. The modes with high $k_\perp$ are then intermittent, and as they contribute the most to energy dissipation, the time series of energy dissipation power is intermittent.

Events.—Statistics issued from observations often involve the detection of events, or structures, from the observed fields (Aschwanden et al. 2000; Parnell & Jupp 2000; Buchlin et al. 2006) and the distributions of their characteristics. Following the "threshold" definition of Buchlin et al. (2005), with a threshold fixed at the average dissipation power, we obtain the distributions shown in Figure 12 for the event total energy content, the peak power of energy dissipation, the duration of events, and the waiting time between two successive events.

The distribution of the peak power in events is narrow, as a result of the summation of the heating function over the whole loop: the local spikes of energy dissipation are hidden by the average dissipation occurring in the whole loop. On the other hand, the distributions of integrated dissipation power (total energy content of events) and of event duration are very wide. This is partially due to the threshold definition used (Buchlin et al. 2005) in the case of this time series, where long timescales are superposed on the shorter timescales of energy dissipation in the dissipative range. Furthermore, the waiting times between successive events also have a wide power-law distribution. However, as discussed extensively in Buchlin et al. (2005), this result depends on what definition of an event is used to extract events from the time series of the power of energy dissipation.

Compared with the distributions of events obtained from the loop shell model of Nigro et al. (2004), the main difference is the much steeper slope (−4.9 instead of −1.8) of the distribution of the peak power in events. The reason could be the summation effect due to the existence of more but smaller dissipation events along the loop, because of the higher resolution we used in this run, both along the loop ($n_z = 2000$ instead of $n_z = 200$, allowed

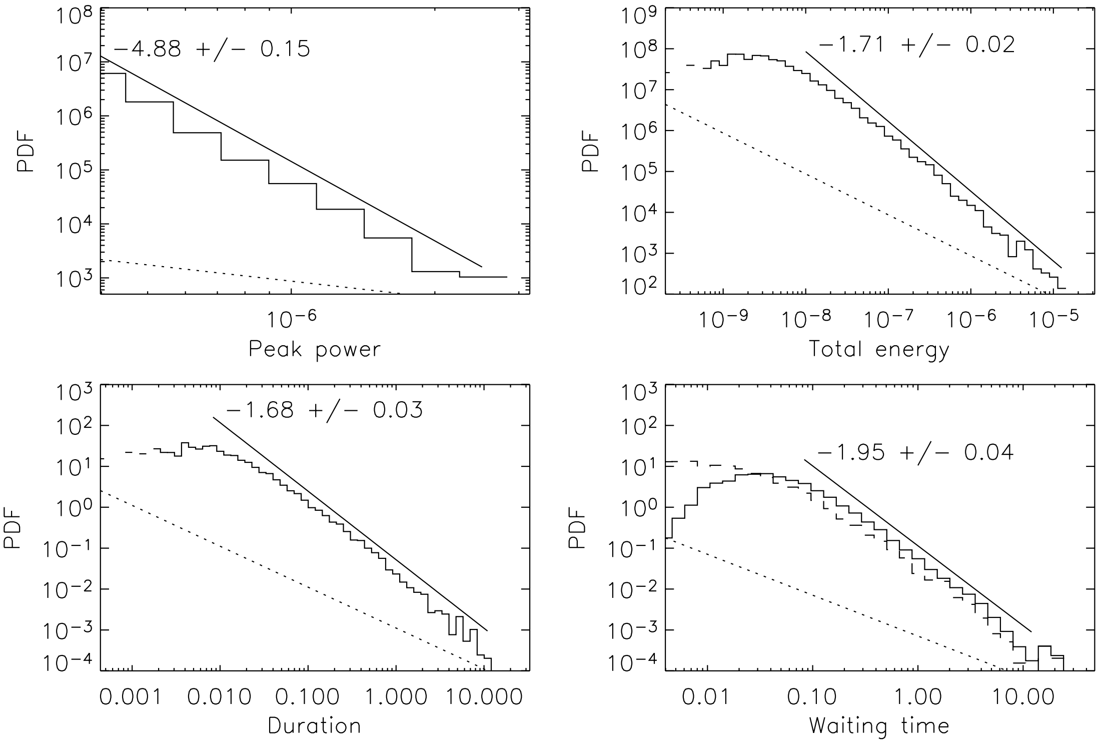

FIG. 12.—Distributions of peak power, total energy content, duration, and waiting times for events found in the time series of energy dissipation power. The dotted lines represent one event per histogram bar.

by the parallelization of our code) and in the perpendicular direction ($n_\perp = 16$ instead of $n_\perp = 11$).

3.4. *Frequencies and Time Correlations*

3.4.1. *Frequencies*

The time series of the kinetic and magnetic energies reveal oscillations corresponding to an exchange of energy between the velocity and magnetic fields. These exchanges occur, for example, thanks to the crossing of Z^+ and Z^- wave packets and should have periods that vary depending on the precise number and repartitioning of wave packets along the loop. A characteristic timescale is of course given by the Alfvén crossing time $\tau_{\rm A,\,max}$, corresponding to the first resonance frequency $f_0 = 1/\tau_{\rm A,\,max}$. Multiples of the Alfvén crossing time correspond to higher frequency resonances of a loop in linear theory. While the power spectrum of the time series of total energy is a power law of index -2 over more than 4 decades, the spectra of magnetic and kinetic energy display peaks corresponding to these resonances. The spectrum of the time series of kinetic energy (Fig. 13) fits to a power law of index -2.5 at very low frequencies. The first resonant frequency, together with the higher frequency harmonics, appear as peaks overlying a different, steeper power law for the higher frequencies, as shown in the bottom panel of Figure 13. The frequencies of the peaks correspond well to integer multiples nf_0 of the fundamental for $n \geq 5$, while at lower frequencies they appear shifted. This shift, which is absent in a linear simulation (realized with the same parameters but without shell models, i.e., with no nonlinear interactions), is probably due to anharmonicity introduced by the nonlinear effects, as shown by Milano et al. (1997) and Nigro (2005).

An even better understanding of these oscillations may be gleaned from a time-frequency analysis by means of a wavelet transform, shown in Figure 14: there are oscillations that have long but finite lifetimes and different frequencies dominantly around the fundamental harmonic. These oscillating high-frequency wave packets appear to arise in association with dissipation bursts, seen in the dissipation power time series (Fig. 14, *bottom*). This intermittent rise in the high-frequency component of the velocity field may be involved in the enhanced nonlinear interactions required to generate the bursts in power, as required in the flare-driving mechanism highlighted by Nigro et al. (2005). On the other hand, their persistence may be related to excitation by the time-space localization of the bursts themselves, a sort of post-microflare resonant ringing, which might be observable with future high-cadence spectroscopic measurements.

The comparison between the spectra of the forcing function at a boundary and of the resulting energy time series (Fig. 13, *top*) makes it clear that the spectrum of energy is not contaminated by the spectrum of the forcing function, as the latter only contains very low frequencies, at or below $1/t^*$; this may not be the case with a stochastic forcing function such as the one used by Nigro et al. (2004). This underscores the role of turbulence in providing the high frequencies that can resonate in the loop, viewed as a cavity for Alfvén waves, even in the absence of an external driver at these frequencies.

3.4.2. *Autocorrelations*

The correlation time of the energy time series is a few dozen Alfvén wave loop crossing times (Fig. 15), consistent with the slow evolution of the energy that we have already noted. The correlation time of the dissipation power time series is shorter, but it is still longer than the wave crossing time, as an effect of the weakness of the intermittent nonlinear interactions between counter-propagating wave packets and of the global long-term fluctuations of the spectrum (including the dissipative range) noted in § 3.2.2.

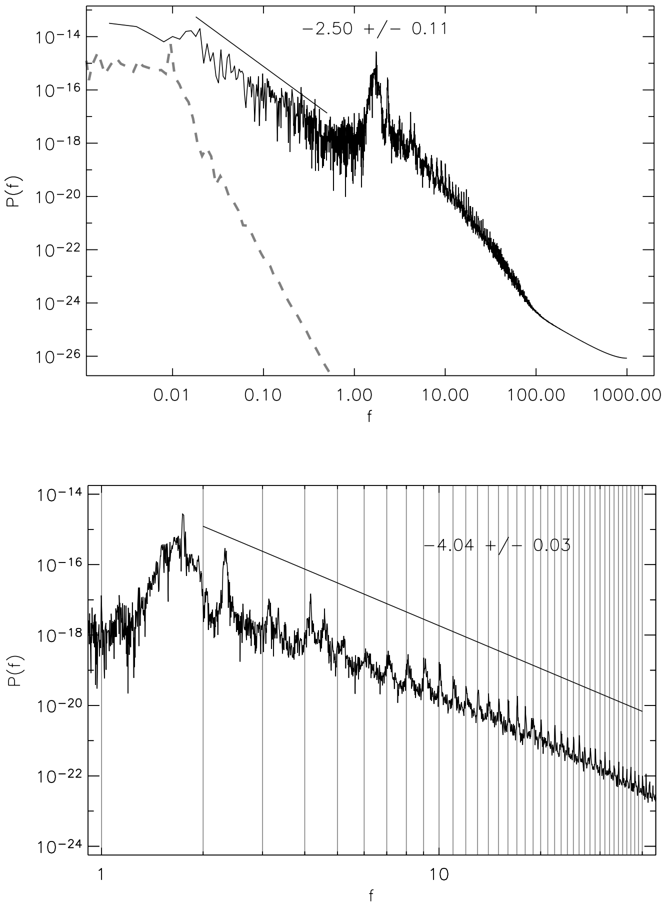

FIG. 13.—Spectrum of the time series of kinetic energy (*solid black curves*). The bottom panel is a zoom on the high-frequency range of the spectrum, where vertical lines represent the harmonics of the first resonant frequency, $f_0 = 1$. Power-law fits and the slopes obtained are superposed; the horizontal range of the lines indicates the range of the fits, and they are shifted vertically for clarity. The spectrum (in arbitrary units) of the square amplitude of the forcing function $[|u_{0,n}(t)|^2$ from eq. (9)] is superposed in the top panel (*dashed gray line*).

3.4.3. *Cross-Correlations*

A common goal when studying solar flares and space weather is to find precursors of flares, so as to make forecasts of possible solar-terrestrial events (e.g., Abramenko et al. 2002; Abramenko 2005; Georgoulis 2005). With this heating model, we can use the cross-correlations between time series to investigate which time series react first, and what kind of observations would be helpful when predicting flares. We have extended the study of Nigro et al. (2005), who show that in some events the kinetic energy begins to grow just before the start of a dissipation event, by performing a systematic correlation study between all energy and dissipation time series (kinetic, magnetic, and total). Figure 15 shows the cross-correlations between the dissipation ϵ and the energy E time series, as well as between the dissipation ϵ and the kinetic energy E_u time series.[5] Both cross-correlation functions show delays of the dissipation compared with the energy: the dissipation lags by approximately 5 time units compared with the total energy, and by approximately 0.5 time units compared with the kinetic energy (this last result is a confirmation of the result obtained by Nigro et al. 2005). Thus, diagnostic methods based on the total energy or including magnetic field measurements may provide more useful results for space weather prediction than methods based on the velocity field alone. However, in both cases the delays involved are short, on the order of a minute at best.

3.5. *Parametric Study of Dissipation Power*

Using the same runs as in § 3.1.2 (a set of loops with different aspect ratios for a fixed width), we compute the average energy dissipation in a stationary state and plot it versus the aspect ratio (Fig. 16): the energy dissipation power per unit volume scales approximately as $a^{-3/2}$. This scaling can be compared with the different models listed by Mandrini et al. (2000) and corresponds to heating from two-dimensional MHD.

As the slope of this power-law scaling is steeper than -1, shorter loops are more efficient in terms of dissipation power per unit surface. This can be explained by the fact that Alfvén wave packets that reflect on the loop footpoints interact more frequently in a short loop than in a long loop; as a matter of fact, simulations performed with varying Alfvén speed show that the average dissipation power also increases when the Alfvén speed increases. Assuming that the physical units of the model (see § 2.4) are 10 Mm, 5 s, and 10^9 kg, yielding $l = 1$ Mm, $b_\parallel = 2$ Mm s^{-1}, and $\rho_0 = 10^{-12}$ kg m^{-3}, we find dissipation powers per unit surface between 10^2 W m^{-2} for large aspect ratios and 10^3 W m^{-2} for small aspect ratios. These values would be sufficient to heat the quiet corona (Withbroe & Noyes 1977). Note, however, that they also depend on the physical properties $b_\parallel$ and ρ_0 that we have assumed for the loop. Another series of runs was performed to explore the influence of $b_\parallel$ on the heating, and it yields $\epsilon_S \propto b_\parallel^{1.77}$; this reflects the fact that wave packets interact more frequently when the Alfvén speed is higher, leading to more dissipation. Both these fits, combined with a dimensional analysis on the variables ϵ_S (dissipation power per unit surface), ρ_0 (mass density), $b_\parallel$ (Alfvén speed), u_f (forcing speed), and a (aspect ratio), yield

$$\epsilon_S = \frac{10^{2.22}}{a^{0.52}} \left(\frac{\rho_0}{10^{-12}}\right) \left(\frac{b_\parallel}{10^6}\right)^3 \left(\frac{10^3 u_f}{b_\parallel}\right)^{1.23} \tag{17}$$

for the dissipation power per unit surface in SI units (W m^{-2}), as a function of the other variables in SI units (kg m^{-3} and m s^{-1}).

4. CONCLUSIONS

We have presented the Shell-Atm model, which is a generalization of shell models (Giuliani & Carbone 1998) with propagation of Alfvén waves along a $\boldsymbol{B}_\parallel$-field, with the further possibility of introducing a longitudinal stratification of physical properties ($\boldsymbol{B}_\parallel$, mass density, flux tube expansion factor). Although the model is simple and includes only simplified physical processes, it has a very interesting complex nonlinear dynamics, and it is fast enough to obtain statistics of its fields and of the heating it produces; the simplifications we made allow one to explore other properties than those accessible to classical direct numerical simulations. While it is not meant to (and cannot) replace DNSs, for example, because of the lack of three-dimensional information on field line topologies, it partially fills the huge gap between the Reynolds numbers in DNSs and in the real corona: although the Reynolds numbers reached in the model, of order 10^6, are still lower than those expected in the corona, this already represents outstanding progress compared with DNSs. Furthermore, this allows us to explore regimes of MHD turbulence that are not accessible to DNSs; for instance, it allows for intermittency to appear in turbulence while having a complete description

---

[5] Other correlations of pairs of time series of kinetic, magnetic, or total energy or dissipations have not been plotted because they are very similar to either of the plotted correlations, as $\epsilon_u \ll \epsilon_b \approx \epsilon$ and $E_u \ll E_b \approx E$.

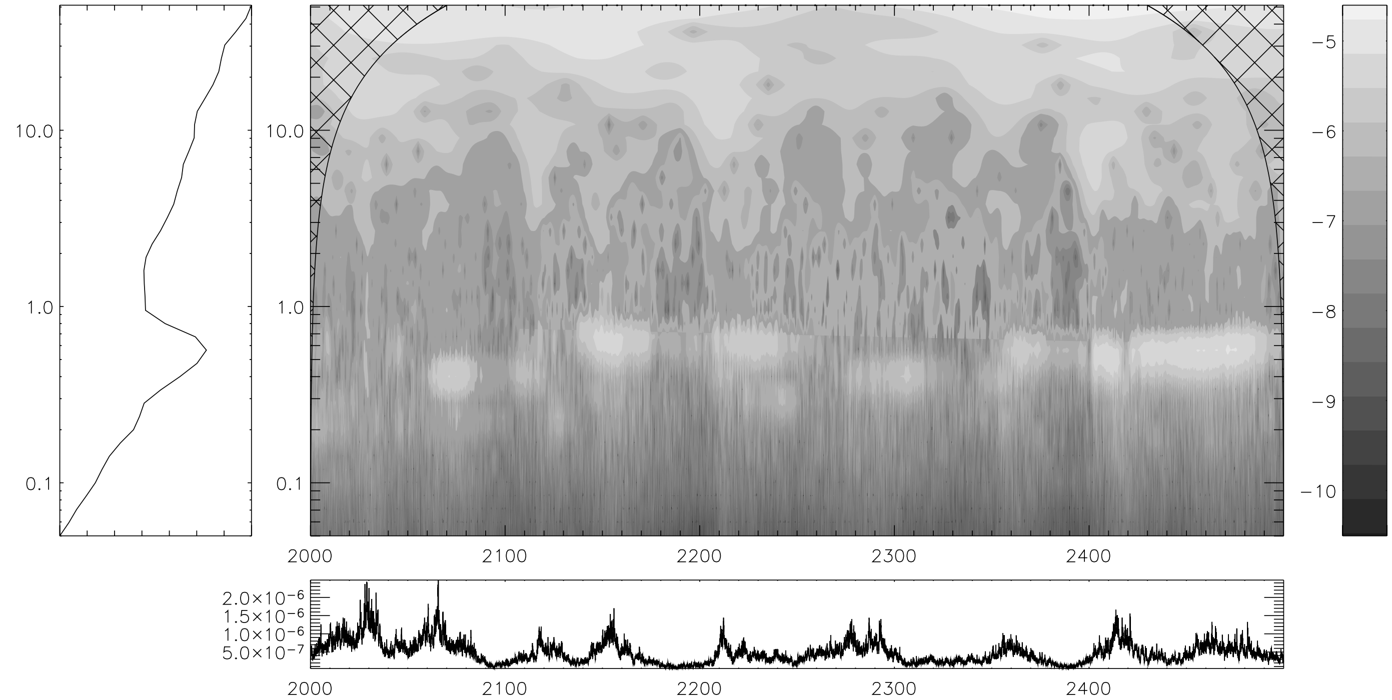

FIG. 14.—*Center*: Morlet wavelet timescale plane of the kinetic energy time series (logarithmic color scale). Oscillations of long but finite lifetime and of different frequencies can be seen at timescales (vertical axis) between 0.2 and 0.6. *Left*: Average wavelet spectrum. *Bottom*: Time series of total dissipation power. [*See the electronic edition of the Journal for a color version of this figure.*]

of the spectra and of the nonlinear interactions in the perpendicular direction. On the other hand, having even higher Reynolds numbers, and thus the smallest scales, may require taking into account non-MHD effects, such as kinetic effects, which can still be neglected in this model.

The model has been used in this paper in the case of a magnetic loop for the solar corona, in which the physical properties of the medium (namely, the external longitudinal magnetic field $\boldsymbol{B}_\parallel$ and the mass density) are assumed to be uniform along the loop. In this case, and thanks to the aforementioned characteristics of the model, we were able to show that this model loop displays a dynamics over a very wide range of spatial and temporal scales (4–5 orders of magnitude); spectra that are formed by a local cross-scale energy flux, and which have a wide inertial range in either direction, perpendicular or parallel to the external magnetic field; a clear anisotropy between the parallel and perpendicular spectra, which could be compatible with the "critical balance" phenomenology; a scaling of the average ratio of the magnetic energy over the kinetic energy consistent with RMHD; a heating function with multiple spatial and temporal scales; a flat longitudinal profile of the average dissipation power (although this may be dismissed by further simulations, with nonuniform physical properties of the medium along the loop); a spiky, and statistically intermittent, time series of energy dissipation power; power-law distributions of the characteristics (peak energy, total energy, duration, waiting times) of "events" extracted from the time series

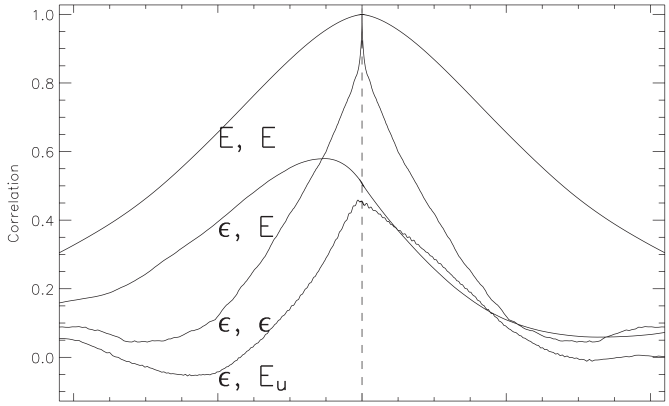

FIG. 15.—Autocorrelation functions and cross-correlation functions of time series of energy and energy dissipation power. E is energy, E_u is kinetic energy, and ϵ is the dissipation power.

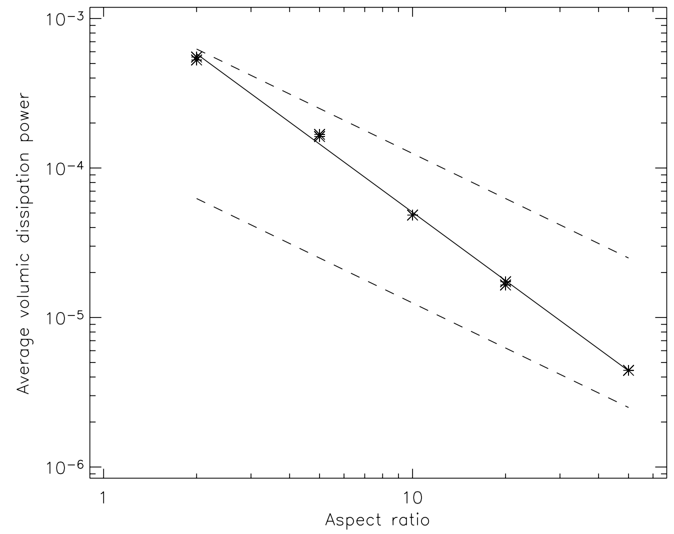

FIG. 16.—Average power of energy dissipation per unit volume (model dimensionless units) vs. aspect ratio a, for a fixed loop width $l = L/a = 0.1$ and external field $b_\parallel = 1$. The power-law fit (*solid line*) has slope −1.52. The two dashed lines represent dissipation powers per unit surface of 10^2 and 10^3 W m^{-2}, respectively.

of dissipation power; finite-lifetime packets of resonant frequencies in the time series of energy, whose frequencies are shifted from the harmonics of the linear resonant frequencies because of the nonlinearities; long-range time correlations in time series; a delay of the dissipation time series compared with some energy time series; and an average dissipation power that scales with the loop parameters and could be sufficient to sustain the high coronal temperatures. As discussed above, some of these results confirm or complete the results of a similar model (Nigro et al. 2004, 2005).

Further directions for the study of the solar corona using this model include taking advantage of the possibility of modeling nonuniform regions (1) to allow for density gradients in a coronal loop, in order to seek for the preferred locations of coronal heating, and (2) to study a magnetically open region such as a coronal hole. In order to obtain diagnostics that can be compared with observations, this heating model can be coupled to the thermodynamics of a loop (including the cooling by conduction and radiation), upon which forward modeling of coronal spectral lines may be carried out. We also believe that this model can be used in other heliospheric and astrophysical applications where MHD applies and where there is a strong dominant magnetic field (see § A3 in the Appendix for code availability).

The authors acknowledge financial support from European Commission grant HPRN-CT-2001-00310 (TOSTISP network). This work was supported in part by NASA grant SHP04-0000-0150. We thank the referee for the suggested improvements to the manuscript. Discussions with S. Galtier and collaboration with A. Verdini when developing the numerical code are greatly appreciated. Part of this work was done while the authors were attending the spring 2005 program Grand Challenge Problems in Computational Astrophysics, at the Institute for Pure and Applied Mathematics, UCLA. The wavelet software was provided by C. Torrence and G. Compo and is available at http://paos.colorado.edu/research/wavelets. Computations were done on Linux clusters at Arcetri Observatory, CINECA, and JPL.

APPENDIX

THE NUMERICAL CODE

A1. NUMERICAL SCHEMES

The time advancement of the nonlinear terms of the shell models is performed with a third-order Runge-Kutta scheme. The Alfvén wave propagation is accomplished with the Fromm (1968) numerical scheme. Finally, the dissipation terms of the shell models can be computed with an implicit scheme. This allows us to relax the CFL condition on τ_ν and thus to fully resolve the dissipative range of the spectrum at no further computational cost.

A2. PARALLELIZATION AND PARALLEL EFFICIENCY

The Shell-Atm model is parallelized using the Message Passing Interface standard, by simply distributing the planes over the processors. Communications are mainly needed for the propagation of the Alfvén waves between the domains corresponding to the different processors, and for the output. The resulting parallelization efficiency is good and is even close to ideal (up to hundreds of processors for $n_z = 10^4$), thanks in particular to effects due to the cache size (when the number of processors grows, the local data become small enough to fit entirely in the level 2 memory cache of each processor).

A3. ARCHITECTURE OF THE CODE AND AVAILABILITY

The Shell-Atm code is modular and can be adapted to a large variety of physical systems. Different models for the nonlinearities and different numerical schemes can be chosen. We believe that the code can be useful for the community, and we have thus released it under the GNU General Public License. The code and its manual can be found at http://www.arcetri.astro.it/~eric/shell-atm/codedoc.

REFERENCES

Abramenko, V. I. 2005, ApJ, 629, 1141
Abramenko, V. I., Yurchyshyn, V. B., Wang, H., Spirock, T. J., & Goode, P. R. 2002, ApJ, 577, 487
Aschwanden, M. J., Tarbell, T. D., Nightingale, R. W., Schrijver, C. J., Title, A., Kenkelborg, C. C., Martens, P., & Warren, H. P. 2000, ApJ, 535, 1047
Aulanier, G., Pariat, E., & Démoulin, P. 2005, A&A, 444, 961
Biskamp, D. 1994, Phys. Rev. E, 50, 2702
Boffetta, G., Carbone, V., Giuliani, P., Veltri, P., & Vulpiani, A. 1999, Phys. Rev. Lett., 83, 4662
Buchlin, E., Aletti, V., Galtier, S., Velli, M., Einaudi, G., & Vial, J.-C. 2003, A&A, 406, 1061
Buchlin, E., Galtier, S., & Velli, M. 2005, A&A, 436, 355
Buchlin, E., Vial, J.-C., & Lemaire, P. 2006, A&A, 451, 1091
Cho, J., Lazarian, A., & Vishniac, E. T. 2002, ApJ, 564, 291
Del Zanna, L., Velli, M., & Londrillo, P. 2001, A&A, 367, 705
Desai, K. M., Gwinn, C. R., & Diamond, P. J. 1994, Nature, 372, 754
Dmitruk, P., Gómez, D. O., & DeLuca, E. E. 1998, ApJ, 505, 974
Dmitruk, P., Gómez, D. O., & Matthaeus, W. H. 2003, Phys. Plasmas, 10, 3584
Frick, P., & Sokoloff, D. 1998, Phys. Rev. E, 57, 4155
Fromm, J. E. 1968, J. Comput. Phys., 3, 176
Georgoulis, M. K. 2005, Sol. Phys., 228, 5
Georgoulis, M. K., Velli, M., & Einaudi, G. 1998, ApJ, 497, 957
Giuliani, P., & Carbone, V. 1998, Europhys. Lett., 43, 527
Giuliani, P., Jensen, M. H., & Yakhot, V. 2002, Phys. Rev. E, 65, No. 036305
Gloaguen, C., Léorat, J., Pouquet, A., & Grappin, R. 1985, Physica D, 17, 154
Goldreich, P., & Sridhar, S. 1995, ApJ, 438, 763
Gómez, D. O., & Ferro Fontán, C. 1992, ApJ, 394, 662
Heyvaerts, J., & Priest, E. R. 1992, ApJ, 390, 297
Isliker, H., Anastasiadis, A., & Vlahos, L. 2000, A&A, 363, 1134
———. 2001, A&A, 377, 1068
Kadomtsev, B. B., & Pogutse, O. P. 1973, Zh. Eksp. Teor. Fiz., 65, 575 (English transl. Soviet Phys.–JETP, 38, 283 [1974])
Kinney, R. M., & McWilliams, J. C. 1998, Phys. Rev. E, 57, 7111
Klein, L. W., Roberts, D. A., & Goldstein, M. L. 1991, J. Geophys. Res., 96, 3779
Kolmogorov, A. N. 1941, Dokl. Akad. Nauk SSSR, 30, 299 (English transl. Proc. R. Soc. London A, 434, 9 [1991])
Lu, E. T., & Hamilton, R. J. 1991, ApJ, 380, L89
Lu, E. T., Hamilton, R. J., McTiernan, J. M., & Bromund, K. R. 1993, ApJ, 412, 841
Mandrini, C. H., Démoulin, P., & Klimchuk, J. A. 2000, ApJ, 530, 999

Milano, L. J., Gómez, D. O., & Martens, P. C. H. 1997, ApJ, 490, 442

Müller, W.-C., Biskamp, D., & Grappin, R. 2003, Phys. Rev. E, 67, No. 066302

Nigro, G. 2005, Ph.D. thesis, Univ. Calabria

Nigro, G., Malara, F., Carbone, V., & Veltri, P. 2004, Phys. Rev. Lett., 92, No. 194501

Nigro, G., Malara, F., & Veltri, P. 2005, ApJ, 629, L133

Oughton, S., Dmitruk, P., & Matthaeus, W. H. 2004, Phys. Plasmas, 11, 2214

Oughton, S., Priest, E. R., & Matthaeus, W. H. 1994, J. Fluid Mech., 280, 95

Parnell, C. E., & Jupp, P. E. 2000, ApJ, 529, 554

Passot, T., & Sulem, P. L. 2003, Phys. Plasmas, 10, 3914

Politano, H., & Pouquet, A. 1995, Phys. Rev. E, 52, 636

She, Z.-S., & Leveque, E. 1994, Phys. Rev. Lett., 72, 336

Shebalin, J. V., Matthaeus, W. H., & Montgomery, D. 1983, J. Plasma Phys., 29, 525

Strauss, H. R. 1976, Phys. Fluids, 19, 134

Velli, M. 1993, A&A, 270, 304

Vlahos, L., Georgoulis, M., Kluiving, R., & Paschos, P. 1995, A&A, 299, 897

Withbroe, G. L., & Noyes, R. W. 1977, ARA&A, 15, 363

Yamada, M., & Ohkitani, K. 1988, Phys. Rev. Lett., 60, 983